# The effects of alkyl substitution on the aggregation of $\pi$-conjugated dyes: spectroscopic study and modelling

Brunella Bardi, Alix Sournia-Saquet, Moreau Alain, Kathleen I Moineau-Chane, Francesca Terenziani

# The effects of alkyl substitution on the aggregation of π-conjugated dyes: spectroscopic study and modelling

Brunella Bardi,[a] Alix Sournia-Saquet,[b,c] Alain Moreau,[b,c] Kathleen I. Moineau-Chane Ching,[b,c,*] Francesca Terenziani[a,*]

A family of dithienosilole-based dyes with alternating donor and acceptor conjugated groups, decorated with linear or branched alkyl chains in different positions of the backbone, has been obtained and investigated in different aggregation states. The dyes are characterized by almost panchromatic absorption and by near-IR emission, with good quantum yields in a variety of solvents with different polarity. We demonstrate that the nature and position of the alkyl substituents strongly govern the self-assembly of the dyes, whose packing is also sensitive to external stimuli, such as grinding and water addition. Thanks to computational results and theoretical modelling, we are able to interpret the results based on two possible preferential packings, characterized by distinct spectroscopic behaviour, whose abundance can be tuned according to the nature and position of the alkyl chains, as well as *via* external stimuli.

## Introduction

Small organic molecules are expected to play a pivotal role in organic electronics, as active materials in devices for light generation and conversion (OLEDs and OPV cells), and the like.[1–7] Their success is related to their numerous advantages over polymeric materials: well-defined structures, low batch-to-batch variability, easiness of purification and functionalization, and good solution processability.[8–11]

Concerning the molecular scaffold, a popular motif consists into the alternation of electron donor (D) and electron acceptor (A) groups joined through conjugated bridges. This approach allows to obtain dyes with intense charge-transfer (CT) transitions in the visible or near-IR, whose position and intensity can be tuned by the number and strength of D and A moieties and their connectivity.[12–14]

Moving from the molecule to the material, made up of several interacting molecules, the degree of complexity increases enormously. Indeed, the optoelectronic properties of molecular assemblies can be strongly affected by the intermolecular interactions, and aggregation may bring about collective and cooperative effects, allowing to obtain larger responses than those achievable with single noninteracting species.[15–20]

Interchromophoric interactions depend upon the supramolecular arrangement that, in turn, is sensitive to several factors. For example, the dye conformation can favor or hinder π-π stacking and can be affected by small modifications of the dye structure, such as the insertion of heteroatoms or bulky groups blocking the molecule in peculiar conformations.[21–24] Even the substitution of just one atom in the molecular backbone can influence the degree of crystallinity in the solid state.[25] Different packings and morphologies can also be achieved when aggregation occurs under kinetic or thermodynamic control, while sample treatments (like annealing) and processing conditions (use of additives, choice of the solvent, operating parameters of film deposition), can all have an enormous impact on the material's properties.[26–30]

The insertion of alkyl substituents is a well-established strategy to increase the solubility of π-conjugated dyes without affecting their optoelectronic properties, since the electronic transitions of aliphatic chains typically occur in the far-UV. However, the presence of alkyl groups can influence the self-assembly ability, film quality, morphology, and stability, modifying in turn charge transport, thermal and optical properties of the material, with repercussions on the device performance.[31–34]

Interestingly, when metastable states are formed, it is sometimes possible to interconvert them or make them evolve towards the thermodynamically stable state with minimal energetic inputs, such as those provided by mild external stimuli, like grinding or heating. If the phase transitions are accompanied by a detectable variation of a macroscopic property, for example the change of the emission color, a stimuli-responsive system is obtained. Stimuli-responsive materials are studied for several applications, e.g. switches, sensors and memory devices.[35–37]

The control on the surface morphology and molecular packing at the nanoscale is fundamental to obtain high performance devices, however it is not easy to realize. Indeed, while the effect of modifications of the conjugated backbone on the

[a] *Department of Chemistry, Life Sciences and Environmental Sustainability, University of Parma, Parco Area delle Scienze 17/a, 43124 Parma, Italy. E-mail: francesca.terenziani@unipr.it*

[b] *Laboratoire de Chimie de Coordination (LCC), CNRS, 205 route de Narbonne, FR-31077 Toulouse Cedex 4, France. E-mail: kathleen.chane@lcc-toulouse.fr*

[c] *LCC-CNRS, Université de Toulouse, CNRS, 31077 Toulouse, France.*

† Electronic Supplementary Information (ESI) available: [details of any supplementary information available should be included here]. See DOI: 10.1039/x0xx00000x

orbital energies and bandgaps can be accurately understood and predicted by computational methods,[38] the supramolecular organization of dyes is hardly predictable, and well-defined relationships between the structure of the molecule and the supramolecular organization of the system are lacking. In this context, the in-depth investigation of model systems with experimental and computational tools can help to devise specific structure-property relationships and to setup rational designs according to the specific needs.

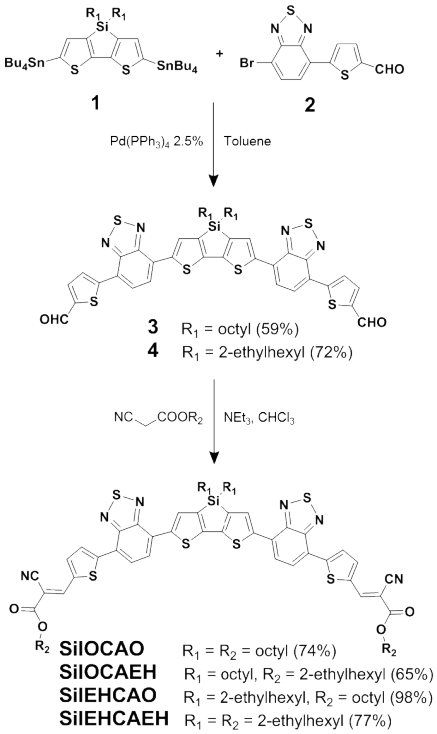


**Scheme 1.** Synthetic route to the target molecules. Yields are indicated for each step.

Here, we build up on our previous works,[39,40] where we studied the packing and stimuli-responsiveness of a few benzothiadiazole-based dyes in different aggregation states. In this work, we explore the self-assembly of some charge-transfer chromophores with a more elongated skeleton properly decorated with aliphatic chains to study the effect of alkyl substitution.

The conjugated backbone of the target dyes consists into an electron-rich heterocycle, dithienosilole, symmetrically substituted with two branches containing an electron withdrawing (benzothiadiazole) and an electron donating (thiophene) group end-capped with a cyanoacetate moiety (Scheme 1). This structure offers two grafting sites, one at the core (dithienosilole) and one at each end (cyanoacetate): for each site, we inserted either a linear (octyl) or branched (ethyl-hexyl) chain, obtaining a series of four different compounds that allowed to address simultaneously the effect of type and location of the substituents.

The chromophores were investigated in solution and in the solid-state, and their aggregation preferences were probed in binary mixtures of solvent/antisolvent of different composition. The spectroscopic signatures of the aggregates were rationalized through an effective few-state model, bridging the structure of the aggregate to its optical properties, and allowing to draw more general conclusions on the spectroscopic properties of aggregates made of polar and polarizable dyes.

## Results

### Molecular design and synthesis

The synthetic route and chemical structures of the four molecules are shown in Scheme 1. Starting compounds 4,4'-dialkyl-5,5'-bis(tributyltin)-dithieno[3,2-b:2',3'-d]silole (molecule **1**, with $R_1$ = octyl or 2-ethylhexyl) and 7-bromo-2,1,3-benzothiadiazole-4-carbaldehyde (molecule **2**) were synthesized according to reported procedures.[41,42] The dialdehyde intermediates **3** and **4** were prepared by the Stille coupling catalysed by palladium-tetrakis(triphenylphosphine) in 59% and 72% yields, respectively. The four molecules were prepared via the Knoevenagel condensation in 65% to 98% yields. Synthetic details and characterization by $^1$H NMR, $^{13}$CNMR and mass spectroscopy are reported in Supporting Information.

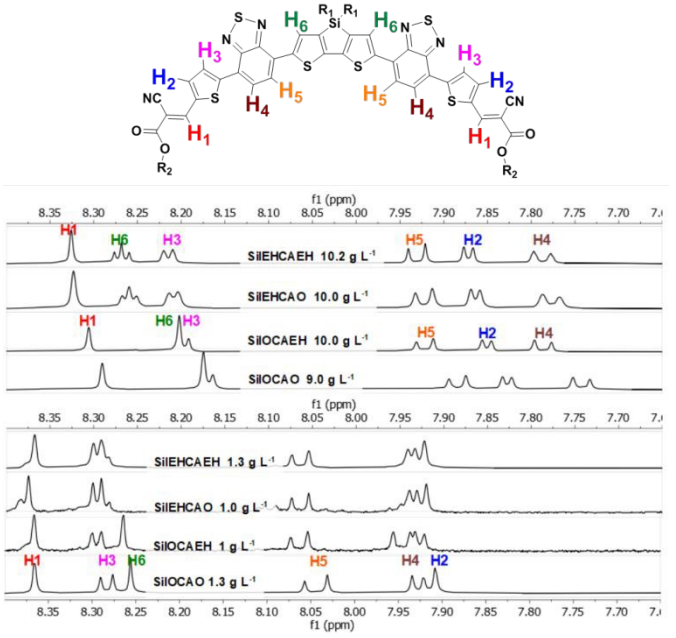


**Figure 1**. $^1$H-NMR spectra from 8.40 to 7.65 ppm of the four molecules in $CDCl_3$ at concentrations around 1 g L$^{-1}$ (bottom) and 10 g L$^{-1}$ (top). Protons numbers on the spectra refer to the labelled hydrogens shown on the above π-conjugated molecular backbone.

### Physicochemical characteristics

**NMR study.** The aromatic part of $^1$H NMR spectra of the four molecules in diluted and concentrated solutions in deuterated chloroform are displayed in Figure 1. Whereas the chemical shifts of the aromatic protons are almost identical for diluted solution (around 1 g L$^{-1}$), they differ significantly for high concentrations (around 10 g L$^{-1}$), indicating a specific role of the alkyl chains depending on their type (linear or branched) and location (central or peripheral). Note that no difference was

observed for the alkyl protons with change in concentration. The variation of chemical shifts for aromatic protons with solvent concentration has been reported for indoles[43] or quinolines[44] and was attributed to molecular aggregation.

In order to get more insight about the specific role of the alkyl chains and their position, we have examined for each molecule the chemical shift vs concentration dependence of the signals of aromatic protons in $CDCl_3$. Figure 2 illustrates the results obtained with **SilOCAO** in 0.1 to 14.5 g $L^{-1}$ $CDCl_3$ solutions (see Figure S1 for the other molecules). The concentration dependent chemical shift changes are linear with negative slopes, and result in overlap/coalescence or crossover of some proton signals.

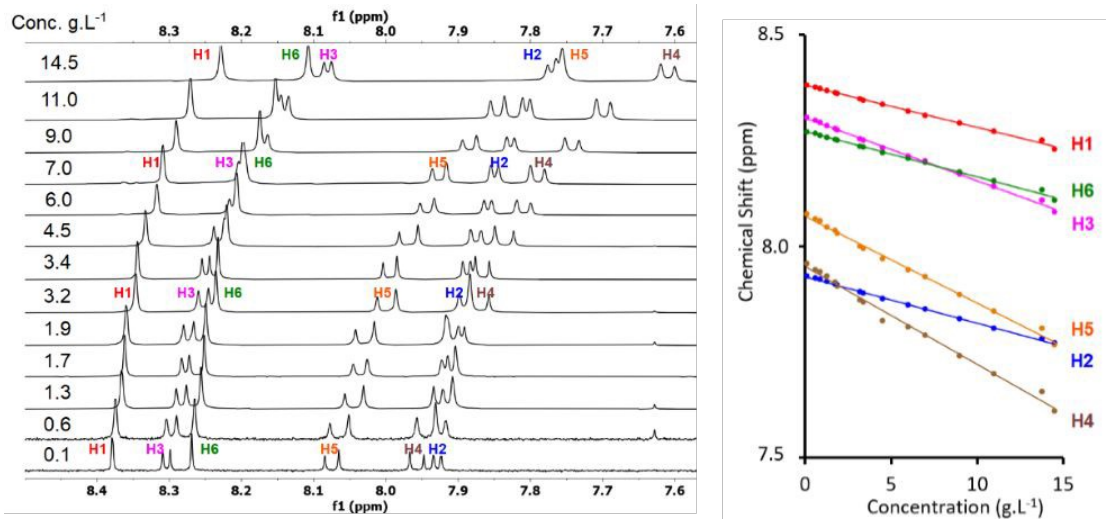


**Figure 2.** Left: aromatic part of $^1$H-NMR spectra of **SilOCAO** at different concentrations in $CDCl_3$. Right: chemical shift versus concentration. Protons numbers refer to the labelled hydrogens shown in Figure 1.

Slope values are specific to each proton, depending on its location on the π-conjugated backbone and depending on the molecule itself, as shown in Figure 3: for a given molecule, protons H4 and H5 are the more affected by concentration increase; H1, H2 and H6 undergo modest and similar changes; the behaviour of H3 is in between. **SilOCAO** is the most sensitive to concentration effect, whereas **SilEHCAEH** is the less one. The slopes values obtained for H1, H2, H3 and H6 for **SilOCAEH** are slightly higher than those for **SilEHCAO**, H4 and H5 being similarly impacted for these two molecules. Protons of **SilEHCAO** and **SilEHCAEH** demonstrate very similar behaviour.

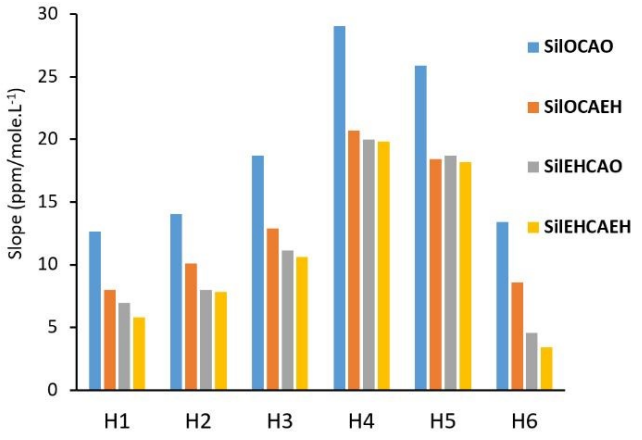


**Figure 3.** Representation of the slope values extracted from concentration dependent chemical shift changes for protons H1 to H6 in $CDCl_3$ for the four molecules.

**Thermal properties.** We probed the thermal properties of these compounds by differential scanning calorimetry (DSC). As shown in Figure S2, the two molecules with octyl central chains (**SilOCAO** and **SilOCAEH**) melt at 207 °C, i.e. 30 °C higher than the two others with ethylhexyl central chains. For **SilEHCAEH**, the wide fusion peak recorded during the first cycle between 180 and 201 °C (not shown here) is split during the following cycles into two transitions at 172 °C and 202 °C, indicating the presence of conformational polymorphs due to thermal treatment. The robustness of the molecules is demonstrated by $^1$H NMR analysis performed on the samples after DSC analyses, that showed no alteration of the molecular structures despite thermal treatment up to 250 °C.

**Electrochemical properties.** The electrochemical behaviour of **SilOCAO** and **SilEHCAEH** was examined by cyclic voltammetry (CV) and square wave voltammetry (SWV) in dichloromethane solutions over a range of potential between -1.2 and 1.6 V/SCE. The two molecules behaved similarly, undergoing two oxidation and one reduction phenomena (Figure 4). The analysis of the electrochemical signals is detailed below for **SilOCAO**, similar results were obtained for **SilEHCAEH**, unless specifically discussed (vide infra).

Figure 5 illustrates, for the oxidation and the reduction couples, the invariance of the value of potential peaks as a function of the scan rate ($v$) along with a linear evolution of the values of the current peak as a function of $\sqrt{v}$. This is consistent with rapid redox processes governed by diffusion in solution, without any chemical reaction or adsorption on the working electrode over these potential ranges.

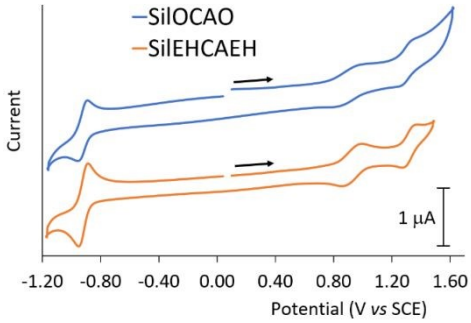


**Figure 4.** Cyclic voltammograms recorded in $CH_2Cl_2$ + $tBu_4NPF_6$ 0.1 mol $L^{-1}$ on platinum electrode at 0.2 V $s^{-1}$. Concentration: **SilOCAO** (blue) $1.01\times10^{-3}$ mol $L^{-1}$ and **SilEHCAEH** (orange) $9.65\times10^{-4}$ mol $L^{-1}$. The arrows indicate the direction of the potential scan.

The mutual examination of the signal recorded at $Ep_{ox1}$ of 0.97 V/SCE in CV (see Figures 4 and 5) and SWV (see Figure 6) reveals a slight enlargement, which is due to two reversible and quasi-superposed single-electron oxidation processes occurring for two distinct systems that do not communicate electrochemically. The shape of the second oxidation wave at $Ep_{ox2}$ of 1.37 V/SCE is typical of a reversible single-electron oxidation ($E_{1/2}$ = 1.31 V/SCE). **SilOCAO** undergoes overall three oxidation processes without degradation up to +1.6 V/SCE.

The reduction wave at $Ep_{red}$ of -0.95 V/SCE corresponds to a reversible single-electron reduction process ($E_{1/2}$ = -0.91 V/SCE). Both **SilOCAO** and **SilEHCAEH** tolerate a mono-electron reduction process without degradation over this range of potential. Below -1.15 V/SCE, the situation is different, depending on the molecules, as illustrated in Figure S3. For **SilOCAO**, a very strong reduction current wave is observed, with a current peak recorded at -1.5 V/SCE; the shape of the signal for the reverse scan is characteristic of a slow redox process with the re-oxidation of species deposited on the electrode. **SilEHCAEH** exhibits no adsorption phenomenon, but undergoes two reversible redox processes very close in potentials, around -1.20 and -1.32 V/SCE.

To resume, the two molecules behave very similarly and reveal an impressive electrochemical robustness over the potential range reachable in dichloromethane, from -1.8 to +1.6 V/ECS. The only difference between the two molecules is in the adsorption phenomena observed for **SilOCAO** for high reduction potentials. Therefore, the octyl chains promote the adsorption phenomenon of the conjugated backbone on the platinum electrode, unlike the ethylhexyl chains.

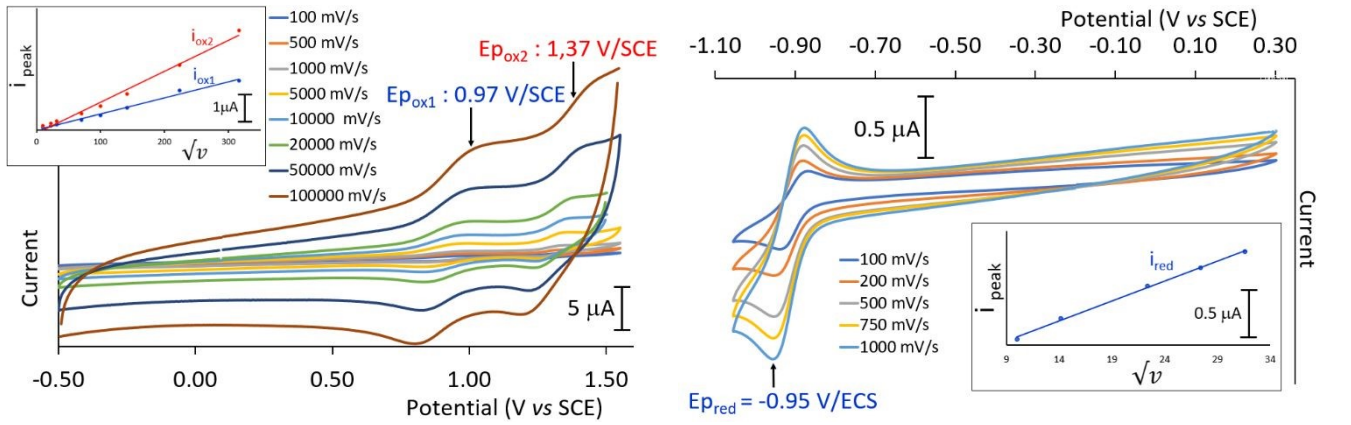


**Figure 5**. Cyclic voltammetry: evolution of the voltammograms obtained for **SilOCAO** $1.01\times10^{-3}$ mol $L^{-1}$ in dichloromethane at different scan rates. Left: oxidation between -0.5 and +1.5 V/SCE. Right: reduction between +0.3 and -1.0 V/SCE. Insets: evolution of the values of current peaks as a function of $\sqrt{v}$.

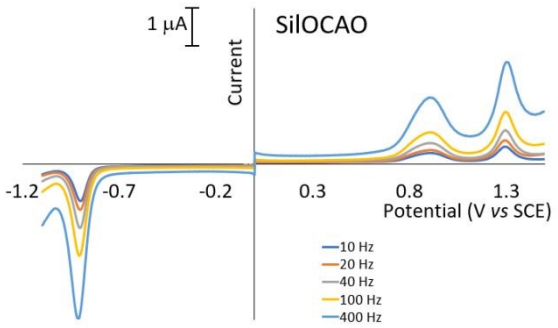


**Figure 6**. Square-wave voltammetry: evolution of voltammograms obtained for **SilOCAO** at different frequencies. square-wave amplitude $E_{sw}$ = 20 mV. On the left: reduction between 0.0 and -1.0 V/SCE. On the right: in oxidation between 0.0 and +1.5 V/SCE.

### Optical spectroscopic characterization

**Solution and solid state.** Absorption and emission spectra of the chromophores in different solvents are presented in Figure 7, while main photophysical parameters are listed in Table 1.

Absorption spectra are dominated by two featureless bands covering most of the UV/vis spectral window, with an offset at $\lambda \approx$ 700 nm. The most intense band spans most of the visible range and has a maximum around 600 nm, while the other extends in the UV and peaks at $\lambda \approx$ 400 nm. Fluorescence is broad and occurs in the red/near-IR. Fluorescence quantum yields are moderate (0.2-0.3) in nonpolar solvents, and smoothly decrease as the solvent polarity is increased. The position and shape of the absorption bands are insensitive to solvent polarity, while emission is solvatochromic. Indeed, the emission maximum is shifted by more than 2500 $cm^{-1}$ moving

from cyclohexane to dimethylformamide, and inhomogeneous broadening progressively blurs the underlying vibronic structure.

To get more information on the electronic transitions contributing to the broad absorption bands, we resorted to fluorescence anisotropy. Excitation anisotropies of two representative dyes, **SilOCAO** and **SilEHCAEH**, are reported in Figure S4. Measurements were performed on undercooled (vitrified) 2-methyltetrahydrofuran solutions, to hinder the rotational motion of the solute. Under these conditions, the measured anisotropy provides information on the polarization of the absorption transitions relative to emission. Excitation anisotropy of both dyes reaches a maximum (0.2-0.3) in the long-wavelength edge of the main absorption band, indicating a small angle (25-30°) between absorption and emission dipole moments, as expected for excitation towards the same state involved in emission. Moving to shorter wavelengths, anisotropy decreases smoothly, reaching a minimum (≈ 0) in-between the two absorption bands (450-500 nm), and increases again at higher energies, coming up with another maximum (0.10-0.15) at the secondary absorption peak. This behaviour suggests that many excited states may be present in this spectral window.

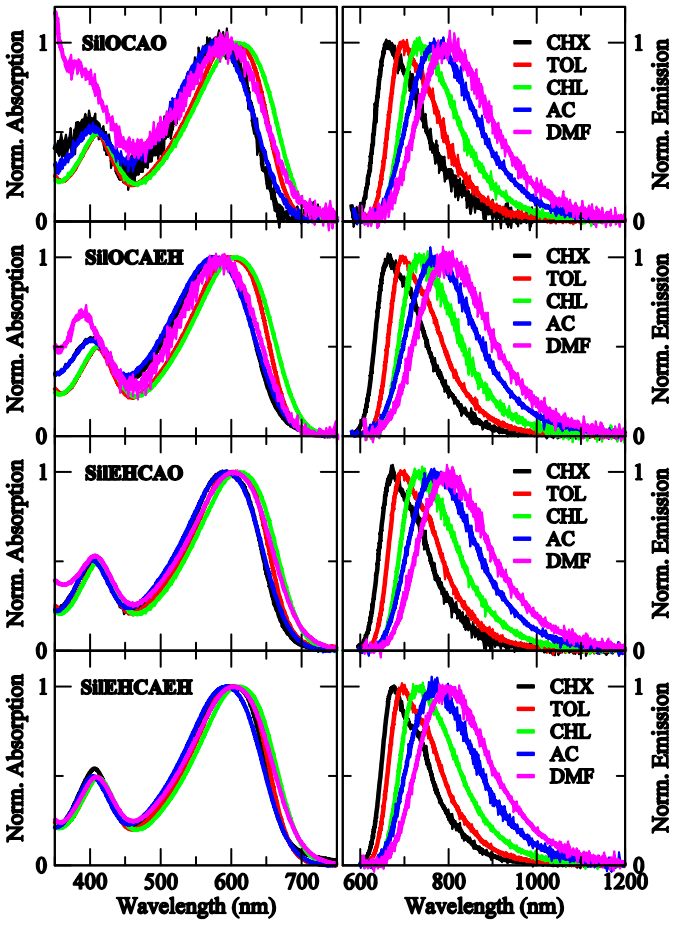


**Figure 7.** Normalized absorption (left) and emission (right) spectra of the chromophores in solvents of different polarity (CHX: cyclohexane, TOL: toluene, CHL: chloroform, AC: acetone, DMF: N,N-dimethylformamide).

**Table 1.** Spectroscopic properties of the chromophores in solvents of different polarity: absorption and emission maxima ($\lambda_{abs}^{max}$ and $\lambda_{em}^{max}$), Stokes shift and fluorescence quantum yield ($\phi$).

| | | $\lambda_{abs}^{max}$ (nm) | $\lambda_{em}^{max}$ (nm) | Stokes Shift ($cm^{-1}$) | $\phi$ [a] |
|---|---|---|---|---|---|
| | Cyclohexane | 581 | 661 | 2080 | 0.27 |
| | Toluene | 600 | 694 | 2260 | 0.30 |
| **SilOCAO** | Chloroform | 606 | 729 | 2780 | 0.25 |
| | Acetone | 582 | 766 | 4130 | 0.16 |
| | DMF | 594 | 802 | 4370 | 0.09 |
| | Cyclohexane | 573 | 663 | 2370 | 0.22 |
| | Toluene | 599 | 696 | 2330 | 0.24 |
| **SilOCAEH** | Chloroform | 606 | 732 | 2840 | 0.21 |
| | Acetone | 576 | 760 | 4200 | 0.13 |
| | DMF | 588 | 802 | 4540 | 0.07 |
| | Cyclohexane | 588 | 675 | 2190 | 0.23 |
| | Toluene | 606 | 692 | 2050 | 0.25 |
| **SilEHCAO** | Chloroform | 612 | 732 | 2680 | 0.20 |
| | Acetone | 594 | 771 | 3860 | 0.12 |
| | DMF | 605 | 805 | 4110 | 0.08 |
| | Cyclohexane | 597 | 676 | 1960 | 0.23 |
| | Toluene | 600 | 695 | 2280 | 0.28 |
| **SilEHCAEH** | Chloroform | 612 | 734 | 2720 | 0.21 |
| | Acetone | 594 | 776 | 3950 | 0.12 |
| | DMF | 606 | 803 | 4050 | 0.07 |

[a] Quantum yields were measured upon excitation in proximity of the absorption maximum. Fluorescence standard: cresyl violet in ethanol ($\phi = 0.51$, $\lambda_{exc} = 550$ nm). DMF: N,N-dimethylformamide.

Further evidence of a complex excited-state scenario is provided by the comparison of the linear absorption (one-photon absorption, 1PA) spectra and the two-photon absorption (2PA) spectra of the two dyes (Figure S5). The lack of inversion symmetry makes all the electronic transitions both one-photon and two-photon allowed, however, their relative intensities in linear and nonlinear processes may differ. Indeed, 1PA and 2PA bandshapes are markedly different: while the 1PA maximum occurs at 600 nm, 2PA peaks at ~530 nm (transition energy), i.e., on the blue side of the main absorption band. The 2PA maximum is close to the anisotropy dip, suggesting the presence of at least another electronic state in-between the two linear absorption maxima giving a larger contribution to 2PA with respect to 1PA. Accordingly, the two 1PA bands, which are very broad also in nonpolar solvents and at low temperature, originate from the superposition of different electronic transitions with different intensity and/or polarization, all contributing in an additive way to anisotropy, 1PA and 2PA.

Spectroscopic investigation of the chromophores was performed also in the solid state, either without pre-treatment of the sample (pristine powders) or after gentle grinding (ground powders). Relevant spectra are shown in Figure 8. Due to the sizeable scattering of pristine samples, absorption spectra were collected for ground powders only.

Emission spectra of pristine powders (Figure 8c) are independent of the excitation wavelength and span the 800-1400 nm range. The position of the maximum depends on the type of alkyl chains grafted to the core: the emission of the two

dyes bearing octyl chains on the dithienylsilyl moiety (**SilOCAO** and **SilOCAEH**) peaks at λ ≈ 1000 nm, while the emission of the dyes with central ethylhexyl substituents (**SilEHCAO** and **SilEHCAEH**) occurs at shorter wavelength (λ ≈ 940 nm). Interestingly, after grinding, the emission of all dyes collapses in the same spectral region (850-875 nm), and the spectral shape is independent of the alkyl-substitution pattern (Figure 8b).

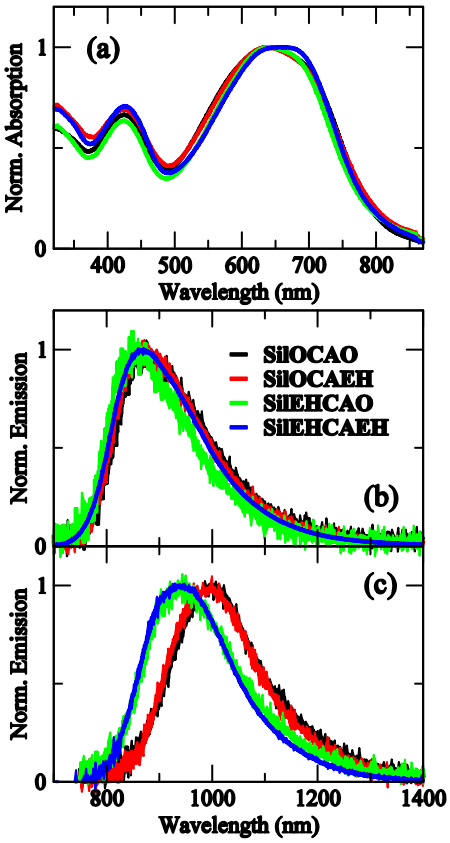


**Figure 8.** Spectra of the chromophores in the solid state. (a) absorption spectra of ground powders; (b) emission spectra of ground powders; (c) emission spectra of pristine powders.

Similarly, the absorption spectra of ground powders of the four dyes are almost indistinguishable from each other (Figure 8a). As in solution, the ground samples feature two main absorption bands: one in the UV (λ ≈ 430 nm) and another, more intense, covering the whole visible spectral range, with an offset at λ ≈ 900 nm. Compared to solution, the former band is slightly red-shifted, while the latter shows a prominent shoulder in the red-edge of the spectrum, between 700 and 800 nm.

The comparison between the emission spectra of pristine and ground powders reveals a mechanochromic behaviour: indeed, grinding induces a displacement of the emission maximum to the blue by 1500 $cm^{-1}$ for **SilOCAO** and **SilOCAEH** and more than 900 $cm^{-1}$ for **SilEHCAO** and **SilEHCAEH**. This behaviour can be related to a rearrangement of the packing, as grinding could provide the energy required to break the (weak) intermolecular contacts of pristine samples.

**Aggregation study in solvent/antisolvent mixtures.** A useful approach to study the self-assembly of chromophores is to force aggregation through the addition of an antisolvent to a solution of the dye in a good solvent. In this work, water was chosen as the antisolvent and tetrahydrofuran (THF) as the solvent, taking advantage of miscibility of the two liquids in all proportions under ambient conditions.

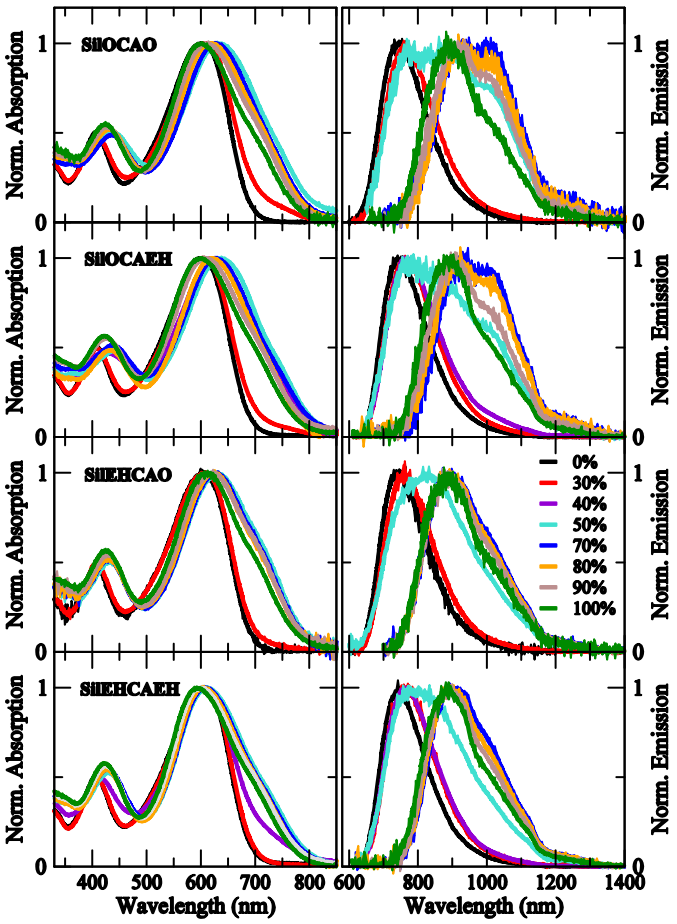


**Figure 9.** Normalized absorption (left) and emission (right) spectra of the dyes in THF/water mixtures of different composition (the percentage of water is reported in the legend). Emission spectra were collected for excitation at the absorption maximum. Sample concentration: 2.0 μmol $L^{-1}$.

Absorption and emission spectra of the dyes in THF/water mixtures with different water content (% in volume) are collected in Figure 9 and reveal an impressive dependence on the mixture composition. In absorption, the presence of water shifts the two bands (the main band at λ ≈ 600 nm and the secondary band at λ ≈ 400 nm) to the red with respect to THF solution and induces the appearance of a shoulder in the red edge of the spectrum, in the 700-800 nm region. The relative intensity of this shoulder, as well as the position of the absolute absorption maximum, changes with the mixture composition.

In emission, the four dyes feature an even more intriguing behaviour. In mixtures containing up to 30-40% of water we can recognize the emission band of THF solution, slightly red-shifted because of the larger dielectric constant. In 50% mixtures, the emission spectrum is exceptionally broad, and three maxima can be identified at λ ≈ 770, λ ≈ 900 and λ ≈ 1000 nm. While the 770 nm peak can still be related to the residual molecules solvated by THF, the other two peaks are indicative of the formation of new (aggregated) species. In mixtures richer in

water (> 50%), the emission band at shorter wavelength vanishes, while the remaining bands change their ratio according to composition. Specifically, the 1000 nm component decreases as the water fraction increases, while the 900 nm component undergoes an opposite trend. The three emission maxima can be tentatively assigned to different concomitant emitting species, whose relative abundance is governed by the THF/water ratio. For convenience, we will hereafter refer to these species as phase I ($\lambda_{em}^{max} \approx 770$ nm), phase II ($\lambda_{em}^{max} \approx 900$ nm) and phase III ($\lambda_{em}^{max} \approx 1000$ nm).

The aggregation behaviour of the four dyes is similar, and the only relevant difference concerns a blue shift of the emission maximum of phase III of **SiIEHX** dyes (**X** = **CAO** or **CAEH**) compared to **SiIOX** dyes. As for pristine powders, dyes differing for the terminal chains are spectroscopically indistinguishable, suggesting a dominant role of the substituents grafted to the molecular core in self-assembly (for a comparison between representative absorption and emission spectra of solution, powders, and THF/water mixtures, see Figure S6).

The striking dependence of the emission bandshape on mixture composition goes along with a sizeable variation of fluorescence quantum yield (Figure S7). The emission of the dyes is moderate in pure THF, as in other solvents with low/medium polarity (Table 1), but it is significantly quenched by water. Indeed, the quantum yield of the samples, starting from $\sim 20\%$ in THF, is almost halved in 30% water mixtures ($\phi \approx 10\%$), and further reduced to 0.5-1% in 50% water mixtures. When water is the main component (> 50%), quantum yields stabilize below 1% and become independent of the mixture composition (within experimental uncertainty).

To figure out the formation of nanoparticles, we characterized the samples by dynamic light scattering (DLS). Only mixtures rich in water (≥ 70%) were examined, as the THF-rich mixtures were poorly scattering and unsuitable for DLS analysis. However, this observation itself suggests that, when the organic component is dominant, solvated monomer is the principal species and aggregates, if present, are less abundant. The addition of water, instead, leads to the formation of nanosuspensions. All samples are highly polydisperse (polydispersity index from cumulant analysis > 0.25), indicating the formation of heterogeneous particles. The size distributions (Table S1) reveal a dominant population with a mean diameter ranging between 40 and 130 nm, and sometimes a minor population of smaller particles (diameter < 10 nm). The dimension of the most abundant population is affected by the mixture composition, in a similar trend for all the dyes, with the biggest particles being formed in 50% water mixtures. Under the same conditions, **SiIEHX** dyes undergo self-assembly into bigger aggregates of similar size, supporting the importance of the role played by the substituents at the molecular core.

More information on the three emitting phases was gathered from the comparative analysis of the excitation and emission spectra collected at different emission or excitation wavelengths. For clarity, we will focus on two representative dyes bearing different substituents at the central site, **SiIOCAO** and **SiIEHCAEH**, and we will consider 50% water mixtures, where all the three emission features are simultaneously present (Figure 10). Excitation and emission spectra of **SiIOCAEH** and **SiIEHCAO**, very similar to those of **SiIOCAO** and **SiIEHCAEH** respectively, are provided in Figure S8.

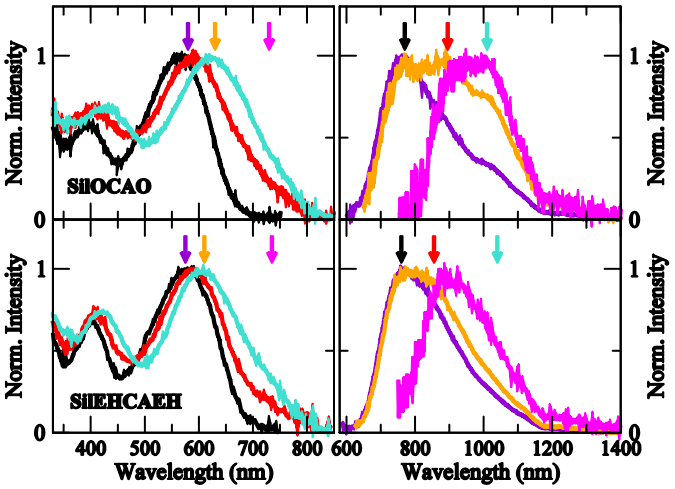


**Figure 10.** Normalized excitation (left panels) and emission (right panels) spectra of **SiIOCAO** and **SiIEHCAEH** in a 50% THF/water mixture, collected for different emission/excitation wavelengths. The emission (excitation) wavelengths are indicated by the coloured arrows in the right (left) panels.

The excitation spectrum collected for detection at the highest-energy emission maximum (λ ≈ 770 nm, black lines) is almost coincident with the absorption spectrum of THF solution, suggesting the identification of phase I with free (solvated) monomer. For detection at the intermediate maximum (λ ≈ 900 nm), the excitation spectrum (red lines) contains the contribution from the absorption of THF solution together with a shoulder in the red characterizing the aggregated phase(s). Indeed, in this region, it is not possible to collect selectively the emission of phase II, as it overlaps with the emission of phases I and III. Finally, for detection at the lowest-energy maximum (λ ≈ 1000 nm) or below, the excitation spectrum (turquoise line) coincides with the absorption spectrum of the sample.

The contribution of the different phases to the absorption/excitation spectrum are more difficult to resolve because of the broad bands. For excitation near the maximum of the solution-like band (λ < 600 nm, violet line), a dominant emission from phase I is observed, together with a tail at longer wavelengths due to the (partial) simultaneous excitation of phase II and/or III. For excitation between 600 and 650 nm (orange line), i.e. close to the absolute absorption maximum of the mixture, all the emission signals are recovered with similar contributions. For excitation at wavelengths longer than 700 nm (purple line), only the signals of phases II and III are obtained, while the contribution of phase I vanishes. This peculiar wavelength-dependence of emission suggests that phases II and III absorb at similar or lower energy compared to phase I and are responsible for the broadening of the main absorption band and the appearance of the red-sided shoulder.

When water is the main component (> 70%), excitation spectra become independent of the emission wavelength and are superimposable to the corresponding absorption spectra. This could be due to the sizable overlap between the emission

spectra of phases II and III, which hampers the selective collection of emission from one of them. Efficient (almost quantitative) excitation energy transfer from phase II to phase III could be an alternative explanation, however it requires more stringent conditions, such as short distance, i.e., the coexistence of both phases inside the same particle, and spectral overlap between the emission spectrum of II and the absorption spectrum of III.

To investigate the evolution of aggregation with mixture composition, we resolved the contributions of the three phases through a fitting of the fluorescence spectra of two representative dyes, **SilOCAO** and **SilEHCAEH**, with a sum of Gaussian functions (details in the ESI). We analysed the spectra collected for excitation at the absorption maximum, to have all the emission features (Figure S9 and S10, and Table S2). For both dyes we satisfactorily fitted the experimental data at all compositions accounting for three Gaussian functions: one peaking at ~ 12700 $cm^{-1}$ (λ ≈ 790 nm), contributing only to 30% and 50% mixtures and roughly corresponding to phase I emission, one at ~ 11300 $cm^{-1}$ (λ ≈ 890 nm) and another at ~ 9900 $cm^{-1}$ (λ ≈ 1010 nm), both present in mixtures > 30% and corresponding to the emission of phase II and phase III, respectively. Comparing the functions obtained for different compositions (Figure S9 and S10, lower panels), we notice that, as the water percentage is increased, the contribution of phase I loses intensity and vanishes, while the contribution of phase II increases and the contribution of phase III decreases concomitantly. Assuming that the quantum yield of the different species is independent of the mixture composition, these results suggest a different stability of the aggregated phases and the possibility to tune their relative abundance through the choice of the solvent/antisolvent ratio.

## Discussion

NMR study of the aromatic part of the chromophores highlights that aggregation phenomena induced by the increase of concentration in $CDCl_3$ does not affect each proton in the same extent. Protons H4 and H5, situated in the central part of the aromatic backbone and in the opposite sites of the alkyl chains, are particularly affected, contrarily to H6 which is in close proximity with the central silicon atom bearing the chains and to H1 and H2 situated at the extremity of the aromatic backbone. Therefore, raising concentration in $CDCl_3$ does not lead to pure π-π stacking (which would affect all protons in the same manner), but to differently packed supramolecular assemblies, as reported for molecules of similar shape which form J- or H-aggregates.[45] Comparison between the four chromophores indicates that aggregation phenomena are the strongest for the molecule bearing only octyl chains (**SilOCAO**). Replacing them by ethylhexyl chains results in dramatic changes, demonstrating that branched chains are less favourable to aggregation. Moreover, examination of the two pairs, **SilOCAO** and **SilEHCAO**, bearing octyl chains in the edge parts, and **SilOCAEH** and **SilEHCAEH**, with ethylhexyl chains, indicates that the nature of alkyl chains grafted in the central part of the chromophore is of noticeable influence on aggregation.

Thermal properties of the four molecules corroborate this conclusion, since the two molecules bearing octyl chains in the central part melt 30 °C above the other two bearing ethylhexyl chains. This suggests that the intermolecular interaction and crystallinity of **SilOCAO** and **SilOCAEH** decrease with the hindrance of the alkyl chains on the central side groups of **SilEHCAO** and **SilEHCAEH**.

Electrochemical studies show that **SilOCAO** and **SilEHCAEH** molecules support three oxidation processes up to a potential value of 1.6 V/ECS without degradation or adsorption. In reduction, while **SilEHCAEH** proves to be electrochemically stable down to potential values of -1.6 V/ECS, **SilOCAO** exhibits adsorption phenomena on the platinum electrode below -1.15 V/ECS. Whereas the ethylhexyl chains prevent the **SilEHCAEH** molecule from adsorption of the π-conjugated system on the platinum electrode, the octyl chains do not oppose this phenomenon.

In solution, the four dyes possess similar spectroscopic properties. Indeed, at low concentrations, the molecules are non-interacting, and their optical properties are mainly governed by their π-conjugated backbone. At this stage, density functional theory (DFT) and its time-dependent extension (TDDFT) can be exploited to support experimental data through a detailed description of the electronic structure of the chromophores.

The conjugated groups can rotate around the bridges, giving rise to many conformational isomers. Because of the small rotational barriers and low relative energies, many conformers are accessible at room temperature and can coexist in solution or even in the aggregates and/or in the solid state.[23,46–49] A detailed conformational study is however beyond the scope of this work so that we focused on only two conformers (***a*** and ***b***, Figure S11), differing by the orientation of the thiophene-cyanoacetate segments. The equilibrium geometries are nearly planar, ensuring high charge delocalization across the molecular backbone (see frontier molecular orbitals in Figures S12 and S13) and allowing to establish close contacts in the solid state.

The excited-state scenario of the dyes was explored *via* TDDFT (Table S3, Figure S14) and is basically independent of the conformation. The $S_0 \rightarrow S_1$ transition corresponds to a HOMO→LUMO excitation, is polarized along the direction of conjugation and has a huge oscillator strength, making it the main contributor to the lowest-energy absorption band. The inspection of the orbitals involved in this transition (Figures S12 and S13) points out a clear CT character. The $S_0 \rightarrow S_2$ transition is found at higher energy ($\sim 0.4$ eV higher), has a low oscillator strength (almost one order of magnitude lower than the $S_0 \rightarrow S_1$ ), and the associated transition dipole moment lies along the $C_2$ axis of the molecule. Accordingly, this transition is likely responsible for the anisotropy dip and the 2PA maximum, in agreement with experimental data. Many closely spaced transitions of comparable intensity and different polarization are found at higher energy, all contributing in a cumulative way to the secondary absorption band.

The spectroscopic properties of the dyes are strongly dependent upon the aggregation state (Figure S6). For all chromophores, the addition of water to a THF solution promotes the spontaneous formation of aggregates. As far as THF is the dominant component (≤ 50% water), a residual solution-like phase (phase I) is present, characterized by the same absorption and emission spectra of the non-interacting molecules in the pure solvent and good quantum yield (> 10%). The addition of water induces the formation of at least two aggregated phases (phase II and III), which are poorly fluorescent and are dominant in water-rich mixtures. Their contributions to absorption cannot be resolved because of the broad and overlapping bands, however, they can be recognized in emission, where they are characterized by distinct maxima. The spectroscopic signatures of phases II and III are independent of the THF/water ratio. Indeed, the mixture composition affects their relative abundance, with the formation of phase II being favoured by water.

The emission of phase II strongly resembles the emission of ground powders, while the emission of phase III finds a remarkable correspondence with the emission of pristine powders. Therefore, we can hypothesize that in solution and in the solid state the dyes arrange according to the same two packing motifs. Phase III may be more crystalline or characterized by longer and/or 3D extended stacks compared to phase II. In the solid state, the energy provided by mechanical action could (partly) break the weak intermolecular contacts converting almost quantitatively phase III into phase II. Conversely, in the THF/water mixtures, the organic solvent, establishing favourable interactions with the solute, could assist the ordering of the molecules into phase III, making sense of the reduction of phase III contribution when increasing the water fraction.

The nature (linear or branched) and location (central or peripheral) of the alkyl chains is irrelevant as far as the dyes are studied in dilute solution. However, the presence of aliphatic groups is fundamental to control the aggregation pattern of the molecules in the solid state and in nanosuspensions, in a similar fashion for all the investigated dyes. A closer look at emission spectra suggests some differences between the chromophores, which can be grouped in two pairs: **SiIOCAO** and **SiIOCAEH** are spectroscopically indistinguishable, and **SiIEHCAEH** and **SiIEHCAO** behave similarly to each other too. These similarities suggest that the intermolecular interactions are driven by the alkyl substituents grafted to the central moiety. We envisage that the two central chains play a more strategic role in self-assembly: since they are linked to the same atom, their steric hindrance can be crucial in the definition of intermolecular contacts and distances. Indeed, the main difference between **SiIOX** and **SiIEHX** dyes concerns the more ordered phase (phase III), which could be characterized by different interplanar distances, depending on the space required for accommodating linear or branched chains.

To enlighten in a broader context the relationship between the spectroscopic properties of powders and nanosuspensions and the molecular packing, we pursued the theoretical modelling of aggregates. Notwithstanding the presence of many donor (D) and acceptor (A) groups, most of the low-energy transitions possess a CT character and imply a charge migration from the central part of the dye (dithienosilole) towards the two branches (Figure S14). Thus, in a simplified view, the dyes can be considered as acceptor-donor-acceptor (A-D-A) systems. Accordingly, we described the non-interacting dyes through a minimal model accounting for three electronic states, corresponding to the limiting resonance structures (for more details, see ESI).[50] With this model, we were able to accurately reproduce the experimental absorption/emission features of the solvated chromophores (Figure S15, Table S4), proving the reliability and robustness of the approach.

Having validated the model for the single molecule (Figures S15 and S16), we moved to the modelling of an aggregate, starting from a dimer (for computational details, see ESI). We considered two alternative packings, *up-up* and *up-down*, sketched in Figure 11a. In the *up-up* arrangement the donor groups point in the same direction, while in the *up-down* arrangement they point to opposite sides. In both of them, the molecules lie on parallel planes fixed at a distance $z$, and the molecules are displaced horizontally and vertically by $x$ and $y$, respectively. As in solution, we assumed that the molecules are slightly bent ($\alpha = 125°$) and, to reduce the number of adjustable parameters, we fixed their molecular arm to an effective length $l = 8$ Å.

The main results are summarized in Figure 11b-e. In Figure 11b we report the energy of the four lowest-energy excited states calculated displacing one molecule along the $x$ direction for fixed $y$ values (Figure S17 for other $y$). The effect of the interplanar distance $z$ is only quantitative, so that in the discussion we will focus on $z = 5$ Å. Analogous figures for $z = 4$ Å and $z = 6$ Å are provided in the ESI (Figures S18-S20). For small $x$, the lowest excited state ($S_1$), i.e., the Kasha state, is dark, while the first bright state ($S_2$) is shifted to higher energy with respect to the lowest state of the monomer. Thus, the absorption of the aggregate is blue shifted compared to the absorption of the noninteracting molecules and fluorescence is quenched. This is the situation referred to as H-aggregates in the framework of the exciton theory.[51] Conversely, when the dyes are largely displaced along $x$, the Kasha state is bright and red-shifted compared to the monomer, a situation typical of J-aggregates.[52] However, there is also an intermediate region where the first excited state is dark (i.e., emission is forbidden) and absorption is red-shifted, a regime that was already termed as 'non-fluorescent J-aggregates' or 'red-shifted H-aggregates' and missing in the exciton scheme.[18,40,53] As detailed elsewhere,[18,20,40] this regime is specific of polar and polarizable molecules, that readjust their polarity in response to the local electric field generated by the neighbouring dyes (also called mean-field effect) experiencing a significant stabilization/destabilization of the electronic states that adds up to the effect of excitonic coupling.

In Figure 11c we reported the energy difference ($\Delta E$) between the absorption of the dimer and that of the monomer calculated on a $xy$ grid, to explore a wide range of geometries. Blue-shifts of the aggregate's absorption up to 0.2 eV were obtained for $x < 5$ Å, while the highest red-shifts (> 0.15 eV) were found

around $x \approx 10$ Å. There is also a narrow region in which the absorption of the aggregate occurs at the same energy of the monomer, when attractive and repulsive interactions between the two molecules cancel out.

For the same distances, the *up-down* arrangement induces bigger spectroscopic effects. The transition dipole moment associated to the lowest-energy transition (i.e., the one involved in fluorescence), is close to zero for cofacial arrangement and, as the molecules are shifted apart laterally, reaches abruptly its maximum value, indicating a 'switch' from a poorly emissive to an emissive dimer (Figure 11d). The switch from dark to fully allowed transition occurs at larger $x$ compared to the inversion of the $\Delta E$ sign, so that three different regimes can be envisaged, as illustrated in the phase diagrams of Figure 11e. The leftmost region of the diagram corresponds to H-aggregates (blue-shifted absorption and poor fluorescence), the rightmost region corresponds to J-aggregates (red-shifted absorption and optically allowed fluorescence) and the middle region, quite narrow for the *up-up* and larger for *up-down* packing, corresponds to red-shifted and poorly fluorescent aggregates.

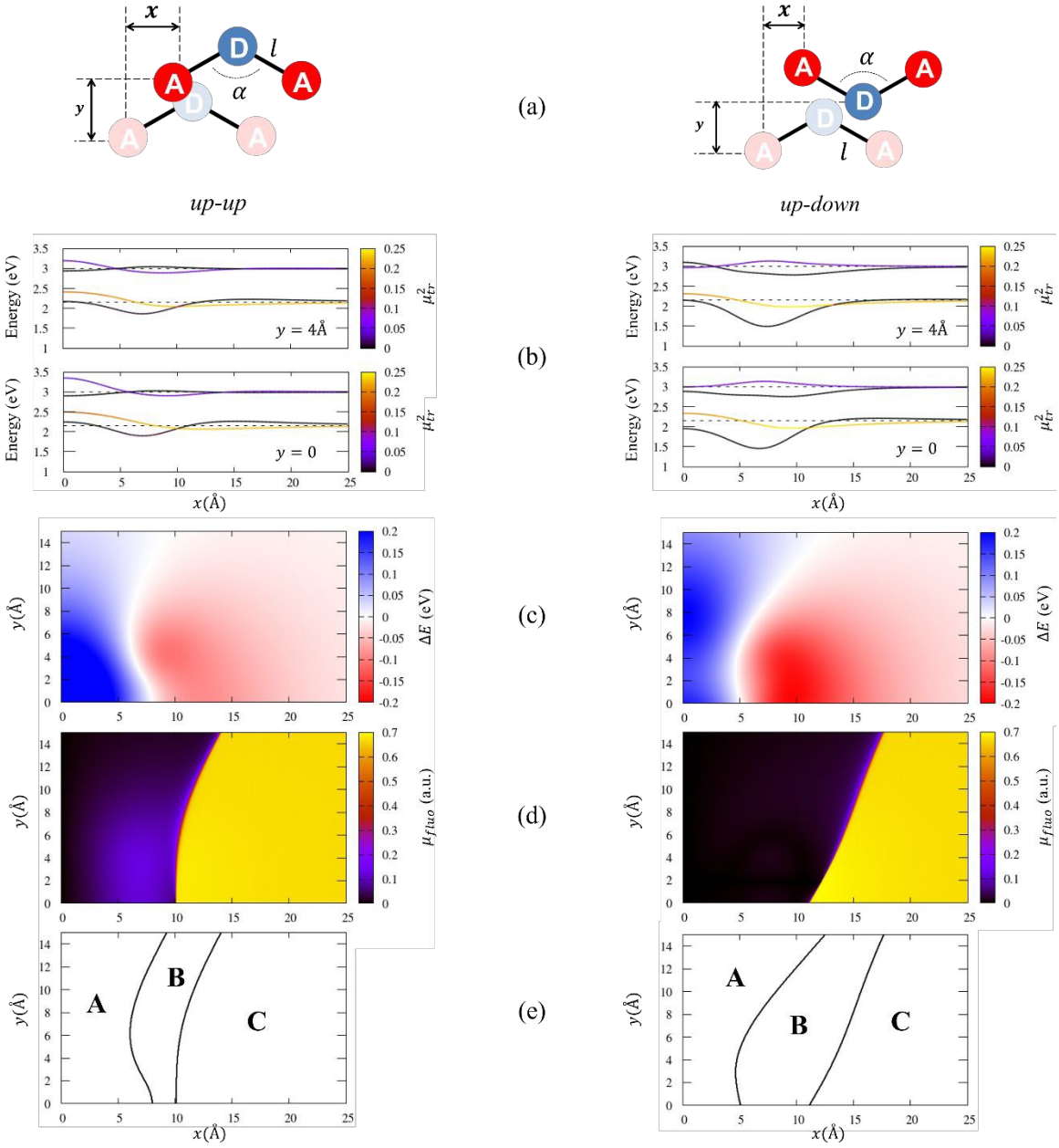


**Figure 11.** Calculated properties of a dimer as a function of the aggregate geometry. (a) Sketch of the *up-up* and *up-down* packings. Blue (red) circles identify donor (acceptor) groups. The molecules lie on parallel planes set at a distance $z = 5$ Å and are displaced by $x$ and $y$ in the other directions. (b) Energy of the lowest electronic excited states as a function of the lateral shift $x$ for selected displacements along $y$. The ground state is taken as the zero of the energy. The colour palette is proportional to the squared transition dipole moment $\mu_{tr}$ from the ground state. Dashed lines mark the transition energies of the monomer. (c) Absorption shift ($\Delta E$) of a dimer as a function of $x$ and $y$. (d) Transition dipole moment associated to emission ($\mu_{fluo}$, dimensionless) as a function of $x$ and $y$. (e) Phase diagram. A: blue-shifted absorption and low-lying dark state (H-aggregates); B: red-shifted absorption and low-lying dark state (non-fluorescent J-aggregates or red-shifted H-aggregates); C: red-shifted absorption and bright fluorescent state (J-aggregates).

In real samples, the situation is more complex. Indeed, nanosuspensions and powders are likely heterogeneous, as a random distribution of conformations and orientations is possible when aggregation occurs under kinetic control. The absorption of the aggregated phases is red-shifted (or at most non-shifted) compared to solution, locating phase II and III either in region B (non-fluorescent J aggregates) or C (J-aggregates) of the phase diagram. Absorption and emission spectra for selected geometries in these two regions and for different numbers of interacting molecules are provided in Figure 12 and S21 for the *up-up* and *up-down* packing respectively. In the *up-up* case, the shift of the absorption maximum of non-fluorescent J-aggregates is low for $y = 0$ and becomes larger when a vertical displacement is introduced. For the *up-down* packing, sizeable red-shifts are obtained event at small $y$. In any case, large Stokes-shifts are observed because absorption and emission originate from different states, and emission intensity is reduced significantly. For J-aggregates, absorption and emission spectra coincide, and fluorescence intensity undergoes a ~10-fold enhancement.

The cofacial stacking ($x = 0$) would imply sizable steric repulsions between the central alkyl chains, so that a lateral shift is more plausible for the target compounds. Indeed, some alkyl-substituted dithienosilole-benzothiadiazole-thiophene dyes were found to crystallize in a slip-stack fashion.[26] The $x = 8$ Å case should be particularly favoured, as the bulky groups are shifted apart minimizing the steric repulsion, allowing for attractive interactions between complementary moieties on the molecular backbones. For non-fluorescent J-aggregates, longer stacks (long-range order), larger vertical displacement of the dyes and shorter interplanar distances, are all factors shifting emission to the red, and can differentiate phase III of **SilOXX** and **SilEHXX** dyes, or even phase II from phase III. It is also possible to observe large emission shifts and monomer-like absorption, a similar behaviour of phase II. J-aggregates, although they seem to be ruled out by the low emission quantum yields, emit at shorter wavelengths compared to their non-fluorescent counterpart, so that their emission could be quenched by energy transfer.

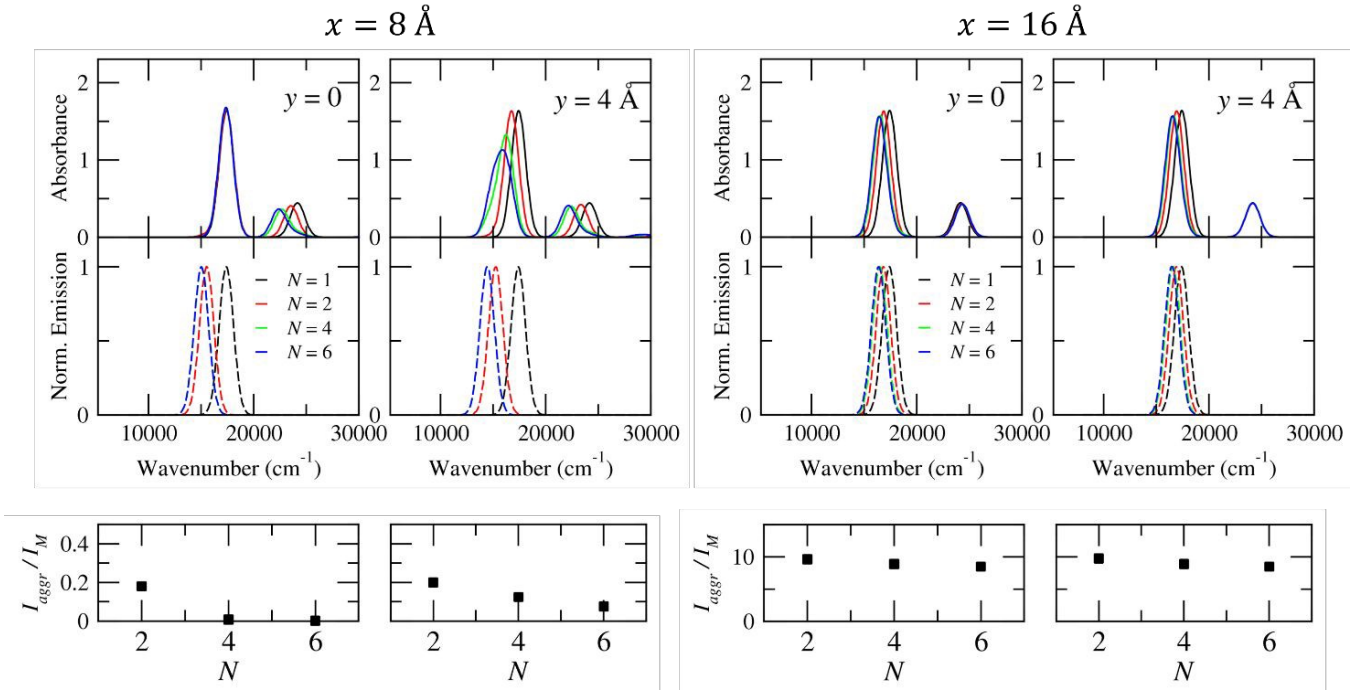


**Figure 12.** Spectra calculated for up-up aggregates of different dimensions ($N$: number of molecules) for $x = 8$ Å and $x = 16$ Å. We set an interplanar distance ($z$) of 5 Å and vertical shift ($y$) of 0 or 4 Å. Top panels: absorption spectra, normalized by the number of molecules. Middle panels: normalized emission spectra. Bottom panels: ratio of the emission intensity of the aggregate, $I_{aggr}$ (integrated area of the spectrum, normalized by the number of molecules) vs the isolated molecule, $I_M$.

## Conclusions

A series of dyes possessing an elongated backbone alternating donor (dithienosilole and thiophene) and acceptor (benzothiadiazole and cyanoacetate) conjugated moieties and decorated with linear or branched alkyl chains both at the core and at the terminal sides were characterized in solution and in different aggregation states. The new chromophores are characterized by many low-energy CT transitions, responsible for an exceptionally broad absorption range (from the UV to ~ 700 nm), and near-IR emission, with good quantum yield over a broad range of solvent polarity. Their emission solvatochromism, combined with the good solubility in different organic media, make them useful as fluorescent polarity probes working for linear and nonlinear excitation over the entire UV/vis spectral window.

The alkyl substituents, which are not involved in conjugation, do not contribute to the low-energy spectroscopy in solution, however, they play a leading role in the self-assembly in the solid state and in nanosuspensions, with impressive effects on the optical properties, highly sensitive to external perturbations (grinding and addition of water). We suggest that the dyes can arrange in at least two preferential forms, poorly fluorescent and characterized by different absorption and emission maxima, whose abundance is controlled by the aggregation conditions. Indeed, with the help of a simple model, we demonstrated that even small variations of the packing geometry can lead to qualitatively and quantitatively different spectroscopic behaviour, so that the insertion of alkyl chains in strategic positions of the conjugated skeleton, thanks to the joint effects of steric repulsion and Van der Waals interactions, is a practical way to control the supramolecular structure and thus the optoelectronic responses of the material.

Indeed, the chosen molecular design allowed to obtain up to three concomitant phases characterized by different emission wavelengths, whose abundance is strongly sensitive to the environment, processing conditions, and mechanical stimuli. The striking responsiveness of such materials would be useful for their application as pressure sensors in the solid state, or as indicators for water content when dissolved in a liquid medium. The theoretical modelling allowed to capture in a non-trivial way the main factors governing the complex interplay between molecular structure, packing and spectroscopy, providing a simplified yet effective framework to rationalize the behaviour of polar/polarizable molecule-based materials and guide the design of smart materials making the most out of multipolar systems.

## Author Contributions

Brunella Bardi: conceptualization, data curation, formal analysis, investigation, methodology, writing – original draft; Alix Sournia-Saquet: data curation, formal analysis, investigation; Alain Moreau: data curation, formal analysis, investigation; Kathleen I. Moineau-Chane Ching: conceptualization, synthesis, data curation, funding acquisition, investigation, methodology, resources, supervision, writing – original draft, writing – review & editing; Francesca Terenziani: conceptualization, funding acquisition, methodology, resources, supervision, writing – original draft, writing – review & editing.

## Conflicts of interest

There are no conflicts to declare.

## Acknowledgements

This work has benefited from the equipment and framework of the COMP-HUB and COMP-R initiatives, funded by the "Departments of Excellence" program of the Italian Ministry for University and Research (MIUR, 2018-2022 and MUR, 2023-2027). This research benefits from the HPC (High Performance Computing) facility of the University of Parma, Italy (HPC.unipr.it).

## Notes and references

1 Y. Sun, G. C. Welch, W. L. Leong, C. J. Takacs, G. C. Bazan and A. J. Heeger, *Nat. Mater.*, 2012, **11**, 44–48.
2 T. S. Van Der Poll, J. A. Love, T. Q. Nguyen and G. C. Bazan, *Adv. Mater.*, 2012, **24**, 3646–3649.
3 B. Kan, Q. Zhang, M. Li, X. Wan, W. Ni, G. Long, Y. Wang, X. Yang, H. Feng and Y. Chen, *J. Am. Chem. Soc.*, 2014, **136**, 15529–15532.
4 Q. Zhang, B. Kan, F. Liu, G. Long, X. Wan, X. Chen, Y. Zuo, W. Ni, H. Zhang, M. Li, Z. Hu, F. Huang, Y. Cao, Z. Liang, M. Zhang, T. P. Russell and Y. Chen, *Nat. Photon.*, 2014, **9**, 35–41.
5 L. Duan, L. Hou, T. W. Lee, J. Qiao, D. Zhang, G. Dong, L. Wang and Y. Qiu, *J. Mater. Chem.*, 2010, **20**, 6392–6407.
6 S. D. Collins, N. A. Ran, M. C. Heiber and T. Q. Nguyen, *Adv. Energy Mater.*, 2017, 7.
7 J. Chen, W. Zhang, L. Wang and G. Yu, *Adv. Mater.*, 2023.
8 J. Roncali, P. Leriche and P. Blanchard, *Adv. Mater.*, 2014, **26**, 3821–3838.
9 Y. Lin, Y. Li and X. Zhan, Chem. Soc. Rev., 2012, **41**, 4245–4272.
10 A. Mishra and P. Bäuerle, *Angew. Chem. - Int. Ed.*, 2012, **51**, 2020–2067.
11 B. Walker, C. Kim and T. Q. Nguyen, *Chem. Mater.*, 2011, **23**, 470–482.
12 F. Bureš, W. Bernd Schweizer, J. C. May, C. Boudon, J. P. Gisselbrecht, M. Gross, I. Biaggio and F. Diederich, *Chem. Eur. J.*, 2007, **13**, 5378–5387.
13 F. Bureš, *RSC Adv.*, 2014, **4**, 58826–58851.
14 T. A. O. Parviainen, P. M. Salmela, R. J. Sippola and J. P. Heiskanen, *ACS Omega*, 2022, **7**, 26328–26335.
15 A. Datta, F. Terenziani and A. Painelli, *ChemPhysChem*, 2006, **7**, 2168–2174.
16 G. D'Avino, F. Terenziani and A. Painelli, *J. Phys. Chem. B*, 2006, **110**, 25590–25592.
17 S. Sanyal, C. Sissa, F. Terenziani, S. K. Pati and A. Painelli, *Phys. Chem. Chem. Phys.*, 2017, **19**, 24979–24984.
18 S. Sanyal, A. Painelli, S. K. Pati, F. Terenziani and C. Sissa, *Phys. Chem. Chem. Phys.*, 2016, **18**, 28198–28208.
19 F. Terenziani and A. Painelli, *J. Lumin.*, 2005, **112**, 474–478.
20 F. Terenziani and A. Painelli, *Phys. Rev. B*, 2003, **68**, 165405–165413.
21 A. Cho, C. E. Song, S. K. Lee, W. S. Shin and E. Lim, *J. Mater. Sci.*, 2016, **51**, 6770–6780.
22 M. Caselli, D. Vanossi, M. Buffagni, M. Imperato, L. Pigani, A. Mucci and F. Parenti, *Chempluschem*, 2019, **84**, 1314–1323.

23 C. J. Takacs, Y. Sun, G. C. Welch, L. A. Perez, X. Liu, W. Wen, G. C. Bazan and A. J. Heeger, *J. Am. Chem. Soc*., 2012, **134**, 16597–16606.
24 G. C. Welch, R. C. Bakus, S. J. Teat and G. C. Bazan, *J. Am. Chem. Soc*., 2013, **135**, 2298–2305.
25 W. Ni, M. Li, F. Liu, X. Wan, H. Feng, B. Kan, Q. Zhang, H. Zhang and Y. Chen, *Chem. Mater*., 2015, **27**, 6077–6084.
26 J. A. Love, C. M. Proctor, J. Liu, C. J. Takacs, A. Sharenko, T. S. Van Der Poll, A. J. Heeger, G. C. Bazan and T. Q. Nguyen, *Adv. Funct. Mater*., 2013, **23**, 5019–5026.
27 M. T. Seifrid, S. D. Oosterhout, M. F. Toney and G. C. Bazan, *ACS Omega*, 2018, **3**, 10198–10204.
28 L. Ye, Y. Jing, X. Guo, H. Sun, S. Zhang, M. Zhang, L. Huo and J. Hou, *J. Phys. Chem. C*, 2013, **117**, 14920–14928.
29 D. Yokoyama, *J. Mater. Chem*., 2011, **21**, 19187–19202.
30 I. K. Kim, J. H. Jo and J. H. Yun, *Nanomaterials*, 2016, **6**, 64.
31 J. E. Coughlin, Z. B. Henson, G. C. Welch and G. C. Bazan, *Acc. Chem. Res*., 2014, **47**, 257–270.
32 W. R. Mateker, T. Heumueller, R. Cheacharoen, I. T. Sachs-Quintana, M. D. McGehee, J. Warnan, P. M. Beaujuge, X. Liu and G. C. Bazan, *Chem. Mater*., 2015, **27**, 6345–6353.
33 B. Tu, Y. Wang, W. Chen, B. Liu, X. Feng, Y. Zhu, K. Yang, Z. Zhang, Y. Shi, X. Guo, H. F. Li, Z. Tang, A. B. Djurišić and Z. He, *ACS Appl. Mater. Interfaces*, 2019, **11**, 48556–48563.
34 K. C. Naeem, K. Neenu and V. C. Nair, *ACS Omega*, 2017, **2**, 9118–9126.
35 Z. Chi, X. Zhang, B. Xu, X. Zhou, C. Ma, Y. Zhang, S. Liu and J. Xu, *Chem Soc Rev*, 2012, **41**, 3878–3896.
36 S. Yagai, S. Okamura, Y. Nakano, M. Yamauchi, K. Kishikawa, T. Karatsu, A. Kitamura, A. Ueno, D. Kuzuhara, H. Yamada, T. Seki and H. Ito, *Nat. Commun*., 2013, 5:4013.
37 Y. Sagara, S. Yamane, M. Mitani, C. Weder and T. Kato, *Adv. Mater.*, 2016, **28**, 1073–1095.
38 L. Pandey, C. Risko, J. E. Norton and J. L. Brédas, *Macromolecules*, 2012, **45**, 6405–6414.
39 B. Bardi, C. Dall'Agnese, K. I. Moineau-Chane Ching, A. Painelli and F. Terenziani, *J. Phys. Chem. C*, 2017, **121**, 17466–17478.
40 B. Bardi, C. Dall'Agnese, M. Tassé, S. Ladeira, A. Painelli, K. I. Moineau-Chane Ching and F. Terenziani, *ChemPhotoChem*, 2018, **2**, 1027–1037.
41 L. Y. Lin, C. W. Lu, W. C. Huang, Y. H. Chen, H. W. Lin and K. T. Wong, *Org. Lett*., 2011, **13**, 4962–4965.
42 C. Chen, D. H. Maldonado, D. Le Borgne, F. Alary, B. Lonetti, B. Heinrich, B. Donnio and K. I. Moineau-Chane Ching, *New J. Chem*., 2016, **40**, 7326–7337.
43 M. G. Reinecke, H. W. Johnson and J. F. Sebastian, *J. Am. Chem. Soc*., 1968, **91**, 3817–3822.
44 A. Mitra, P. J. Seaton, R. A. Assarpour and T. Williamson, *Tetrahedron*, 1998, **54**, 15489–15498.
45 Q. Zhao, X. Yu, J. Liu, Z. Xie and Y. Han, *Org. Electron*., 2016, **37**, 6–13.
46 J. E. Coughlin, A. Zhugayevych, R. C. Bakus, T. S. Van Der Poll, G. C. Welch, S. J. Teat, G. C. Bazan and S. Tretiak, *J. Phys. Chem. C*, 2014, **118**, 15610–15623.
47 M. Reichenberger, J. A. Love, A. Rudnick, S. Bagnich, F. Panzer, A. Stradomska, G. C. Bazan, T. Q. Nguyen and A. Köhler, J. *Chem. Phys*., 2016, **144**, 074904.
48 S. A. J. Thomson, J. Niklas, K. L. Mardis, C. Mallares, I. D. W. Samuel and O. G. Poluektov, *J. Phys. Chem. C*, 2017, **121**, 22707–22719.
49 T. S. Van Der Poll, A. Zhugayevych, E. Chertkov, R. C. Bakus, J. E. Coughlin, S. J. Teat, G. C. Bazan and S. Tretiak*, J. Phys. Chem. Lett.*, 2014, **5**, 2700–2704.
50 F. Terenziani, A. Painelli, C. Katan, M. Charlot and M. Blanchard-Desce, *J. Am. Chem. Soc*., 2006, **128**, 15742–15755.
51 J. Knoester, in Organic Nanostructures: Science and Applications, IOS Press, Amsterdam, 2002.
52 F. Würthner, T. E. Kaiser and C. R. Saha-Möller, *Angew. Chem. – Int. Ed.*, 2011, **50**, 3376–3410.
53 Y. Zhang, B. Kim, S. Yao and M. V Bondar, *Langmuir*, 2013, **29**, 11005–11012.